

A variational multiscale method for inelasticity: Application to superelasticity in shape memory alloys

Arif Masud *, Kaiming Xia

Department of Civil and Materials Engineering, The University of Illinois at Chicago, (MIC 246), 842 W. Taylor Street, Chicago, IL 60607-7023, USA

Received 12 January 2004; received in revised form 26 September 2005; accepted 27 September 2005

Abstract

This paper presents a variational multiscale method for developing stabilized finite element formulations for small strain inelasticity. The multiscale method arises from a decomposition of the displacement field into coarse (resolved) and fine (unresolved) scales. The resulting finite element formulation allows arbitrary combinations of interpolation functions for the displacement and the pressure fields, and thus yields a family of stable and convergent elements. Specifically, equal order interpolations that are easy to implement but violate the celebrated Babuska–Brezzi condition, become stable and convergent. An important feature of the present method is that it does not lock in the incompressible limit. A nonlinear constitutive model for the superelastic behavior of shape memory alloys is integrated in the multiscale formulation. Numerical tests of the performance of the elements are presented and representative simulations of the superelastic behavior of shape memory alloys are shown.

© 2005 Elsevier B.V. All rights reserved.

Keywords: Variational multiscale method; Stabilized formulations; Equal order elements; Nonlinear constitutive models; Shape memory alloys

1. Introduction

This paper presents a new stabilized mixed finite element method for computational inelasticity. The idea of developing stabilized methods for application in computational solid mechanics was motivated by the success of stabilized methods in the arena of computational fluid dynamics. The first applications of stabilized methods to the mixed-field problems can be traced back to the early 1980s [5,13–16] when Hughes and colleagues proposed a generalization of the SUPG method for the Stokes flow problem. The SUPG method turned out to be the fore runner of a new class of stabilization schemes, namely the Galerkin/Least-Squares (GLS) stabilization method [16]. GLS stabilization was soon followed by another class of stabilized methods, introduced by Brezzi, Franca and coworkers [2,4], wherein the idea of augmenting the Galerkin method with virtual bubble functions was employed. Even though the similarity between the mixed $\mathbf{u}-p$ form of incompressible elasticity and the Stokes flow equations was pointed out in Hughes and Franca [14], the application of stabilized methods to incompressible elasticity lagged behind its application to incompressible fluid dynamics.

In the mid-90s Hughes revisited the origins of the stabilization schemes from a variational multiscale view point and presented the variational multiscale method [11]. Since the solid and structural mechanics literature is dominated by variational methods, the variational multiscale method seems to possess a natural affinity for application in solid mechanics. Employing the Hughes' Variational Multiscale method, hereon termed as the HVM method, we developed a new stabilized formulation for incompressible elasticity that is applicable in the incompressible limit [24]. In this paper we present

* Corresponding author. Tel.: +1 312 996 4887; fax: +1 312 996 2426.
E-mail address: amasud@uic.edu (A. Masud).

an extension of the HVM method to the material nonlinear regime and develop a stabilized method for nonlinear solid mechanics [22]. A key idea underlying the multiscale approach is that a given spatial discretization may not be adequate to resolve features in the solution that are smaller than the characteristic length scale associated with the given discretization. In other words, the fine mathematical scales in the solution may not get adequately resolved. This idea leads to a decomposition of the total solution to the governing boundary value problem into two parts, (a) a part that is resolved by the given discretization, and (b) a part that lies outside the resolution capacity of the given mesh and is therefore filtered out. This unresolved part which is the error associated with a given discretization, is also a solution to the governing equation. Accordingly, we perform a substitution of the additively decomposed form of the trial solution and the corresponding weighting function in the Galerkin weighted residual form of the governing equations. The linearity of the weighting function slot leads to two sets of equations. For the case under consideration, these equations are nonlinear because of the nonlinear constitutive relations. Accordingly, linearization of the constitutive model is an integral part of the overall strategy. Once linearized, the fine-scale problem can be solved and the fine-scales can be substituted in the linearized coarse-scale problem, thus leading to a modified problem that is expressed completely in terms of the resolvable scales. Thus, in the context of the present paper, the terminology “scales” means the “mathematical scales” in the solution to the problem.

In the first part of the paper we develop a new mixed stabilized formulation for computational inelasticity. The new formulation possesses several attractive features. Firstly, the structure of the stability tensor τ appears naturally via the solution of the fine-scale problem. Secondly, the present formulation allows arbitrary combinations of interpolation functions for the displacement and the volumetric-stress fields. It is important to note that this property is not shared by the standard Galerkin based mixed formulations that are required to satisfy the Babuska–Brezzi (BB) inf-sup conditions. Thirdly, the present method does not lock in the incompressible limit. A literature review reveals that within the context of the standard Galerkin finite element framework, special techniques are required to develop convergent elements that can address issues related to volumetric constraint. These techniques include the reduced and selective integration methods [3,12,21], stress projection techniques [30,31], mixed methods [17,21], and the B-Bar method [12]. Relatively recently, attempts have been made to employ Petrov–Galerkin method for finite elasticity [18] and for elastoplasticity [8], and multi-scale method for modeling weak discontinuities in solids [9].

In the second part of the paper we integrate a nonlinear constitutive model for shape memory alloys (SMAs) in the stabilized formulation. SMAs are materials that can undergo reversible changes in their crystallographic structure and are able to sustain and recover large strains without inducing irreversible plastic deformations. They can also remember a previous configuration and can return to it with a temperature change. These changes can be interpreted as martensitic phase transformations between a more-ordered phase called *austenite*, and a less-ordered phase, called *martensite*. In the last few years there have been several attempts on the experimental and analytical fronts to understand the micromechanics of SMAs and to develop phenomenological models that are capable of representing the SMA macrobehavior (see e.g., [1,6,7,19,20,23,25,27,28] and references therein). These efforts have resulted in (i) an increasingly detailed information regarding the crystalline structure of SMA materials, (ii) a greater understanding of the macroscopic behavior of SMAs, (iii) the development of new alloys and processing techniques, and (iv) a dramatic increase in the number of applications which now span a wide range of products and devices.

An outline of the paper is as follows. In Section 2, we present a mixed displacement–pressure form for inelasticity. In Section 3 we employ the HVM framework and develop a stabilized formulation for application in computational inelasticity. The novelty of the proposed stabilized formulation is that the structure of the so called stability tensor τ appears naturally in the derivation. Section 4 presents a kinetic cosine model that is capable of representing the experimentally observed superelastic phase transformations under mechanical loading/unloading conditions at constant high temperatures. This kinetic cosine model is a generalization of the linear kinetic model for SMA macrobehavior, presented in Masud et al. [23]. In Section 6, we present a set of numerical examples to verify the theoretical developments and show the range of applicability of the proposed stabilized formulation. Conclusions are drawn in Section 7.

2. A mixed displacement–pressure form for inelasticity

Let $\Omega \subset \mathbb{R}^{n_{sd}}$ be an open bounded region with piecewise smooth boundary Γ . The number of space dimensions, n_{sd} , is equal to 2 or 3. The unit outward normal vector to Γ is denoted by \mathbf{n} . The mixed displacement–pressure form of the governing equations is given as follows:

$$\nabla \cdot \boldsymbol{\sigma} + \mathbf{b} = \mathbf{0} \quad \text{in } \Omega, \quad (1)$$

$$(\boldsymbol{\varepsilon} - \boldsymbol{\varepsilon}^I) \cdot \boldsymbol{\delta} - \frac{p}{K} = 0 \quad \text{in } \Omega, \quad (2)$$

$$\mathbf{u} = \mathbf{g} \quad \text{on } \Gamma_g, \quad (3)$$

$$\boldsymbol{\sigma} \cdot \mathbf{n} = \mathbf{t} \quad \text{on } \Gamma_h, \quad (4)$$

where $\mathbf{u}(\mathbf{x})$ is the displacement field, and $p(\mathbf{x})$ is the scalar field that represents the volumetric-stress, or the hydrostatic pressure in the incompressible limit. $\boldsymbol{\sigma}$ is the Cauchy stress tensor, $\boldsymbol{\varepsilon}^I$ is the inelastic or the plastic strain tensor, and K is the bulk modulus defined as $K = \frac{E}{3(1-2\nu)}$. Eq. (1) represents equilibrium in body Ω , Eq. (2) is the volumetric constitutive equation in Ω , Eq. (3) is the Dirichlet boundary condition on Γ_g , and Eq. (4) is the Neumann boundary condition on Γ_h .

2.1. The standard variational form

The standard variational form of the boundary value problem is stated in terms of the following spaces for trial solutions and weighting functions.

$$\mathcal{S} = \{\mathbf{u} | \mathbf{u} \in H^1(\Omega), \mathbf{u} = \mathbf{g} \text{ on } \Gamma_g\}, \quad (5)$$

$$\mathcal{V} = \{\mathbf{w} | \mathbf{w} \in H^1(\Omega), \mathbf{w} = \mathbf{0} \text{ on } \Gamma_g\}, \quad (6)$$

$$\mathcal{P} = \{p | p \in L_2(\Omega)\}. \quad (7)$$

Because there are no explicit boundary conditions on pressure, \mathcal{P} suffices as both the trial solution space and the weighting function space. The weighted residual form of the equilibrium and the volumetric constitutive equations is as follows:

$$\int_{\Omega} \nabla^s \mathbf{w} : \boldsymbol{\sigma} \, d\Omega = \int_{\Omega} \mathbf{w} \cdot \mathbf{b} \, d\Omega + \int_{\Gamma} \mathbf{w} \cdot \mathbf{t} \, d\Gamma, \quad (8)$$

$$\int_{\Omega} q(\boldsymbol{\varepsilon} - \boldsymbol{\varepsilon}^I) \cdot \boldsymbol{\delta} \, d\Omega - \int_{\Omega} q \frac{p}{K} \, d\Omega = 0, \quad (9)$$

where $\nabla^s(\cdot)$ represents the symmetric gradient operator, and \mathbf{w} and q are the weighting functions corresponding to displacement \mathbf{u} and pressure p , respectively. This is a system of nonlinear equations because $\boldsymbol{\sigma}$ is a nonlinear function of strain, while Eq. (9) contains the inelastic strain $\boldsymbol{\varepsilon}^I$.

3. The variational multiscale method

3.1. Multiscale decomposition

In this section we employ ideas from the variational multiscale method first proposed by Hughes [11], hereon termed as the HVM method, for the development of a multiscale/stabilized finite element formulation for small strain computational inelasticity. We consider the bounded domain Ω discretized into non-overlapping regions Ω^e (element domains) with boundaries Γ^e , $e = 1, 2, \dots, n_{\text{umel}}$, such that

$$\overline{\Omega} = \bigcup_{e=1}^{n_{\text{umel}}} \overline{\Omega^e}. \quad (10)$$

We denote the union of element interiors and element boundaries by Ω' and Γ' , respectively.

$$\Omega' = \bigcup_{e=1}^{n_{\text{umel}}} (\text{int})\Omega^e \quad (\text{elem. interiors}), \quad (11)$$

$$\Gamma' = \bigcup_{e=1}^{n_{\text{umel}}} \Gamma^e \quad (\text{elem. boundaries}). \quad (12)$$

We assume an overlapping sum decomposition of the displacement field into the coarse scales or resolvable scales and the fine-scales or the subgrid scales.

$$\mathbf{u}(\mathbf{x}) = \underbrace{\bar{\mathbf{u}}(\mathbf{x})}_{\text{coarse scale}} + \underbrace{\mathbf{u}'(\mathbf{x})}_{\text{fine scale}}. \quad (13)$$

Likewise, we assume an overlapping sum decomposition of the weighting function into coarse and fine-scale components indicated as $\bar{\mathbf{w}}$ and \mathbf{w}' , respectively.

$$\mathbf{w}(\mathbf{x}) = \underbrace{\bar{\mathbf{w}}(\mathbf{x})}_{\text{coarse scale}} + \underbrace{\mathbf{w}'(\mathbf{x})}_{\text{fine scale}}. \quad (14)$$

We further make an assumption that the subgrid scales although nonzero within the elements, vanish identically over the element boundaries.

$$\mathbf{u}' = \mathbf{w}' = \mathbf{0} \quad \text{on } \Gamma'. \quad (15)$$

Substituting (14) in (8) and exploiting the linearity of the weighting function slot we can split Eq. (8) in a coarse-scale and a fine-scale problem. Without loss of generality we assume that fine-scale pressure $p' = 0$. Accordingly, $q' = 0$ and therefore Eq. (9) only contributes to the coarse-scale problem. Since the trial solutions and weighting functions are implied to be the functions of h , to keep the notation simple, explicit dependence on h is suppressed.

Remark 1. The assumption $p' = 0$ corresponds to the situation wherein volumetric-stress is assumed not to contain the fine-scale features. From a mathematical view point this assumption helps eliminate the fine-scale counterpart of Eq. (9), thus simplifying the fine-scale sub-problem.

The coarse-scale sub-problem:

$$\int_{\Omega} \nabla^s \bar{\mathbf{w}} : \boldsymbol{\sigma} \, d\Omega = \int_{\Omega} \bar{\mathbf{w}} \cdot \mathbf{b} \, d\Omega + \int_{\Gamma} \bar{\mathbf{w}} \cdot \mathbf{t} \, d\Gamma, \tag{16}$$

$$\int_{\Omega} q(\boldsymbol{\varepsilon} - \boldsymbol{\varepsilon}^I) \cdot \boldsymbol{\delta} \, d\Omega - \int_{\Omega} q \frac{P}{K} \, d\Omega = 0. \tag{17}$$

The fine-scale sub-problem:

$$\int_{\Omega} \nabla^s \mathbf{w}' : \boldsymbol{\sigma} \, d\Omega = \int_{\Omega} \mathbf{w}' \cdot \mathbf{b} \, d\Omega + \int_{\Gamma} \mathbf{w}' \cdot \mathbf{t} \, d\Gamma. \tag{18}$$

3.2. Solution of the fine-scale problem

Let us first consider the fine-scale sub-problem. Because of the assumption on the fine-scale \mathbf{w}' given in (15), the boundary term on the right-hand side of (18) drops out. It is important to note that because of the assumption in (15), Eq. (18) is essentially defined over the sum of element interiors. The general idea at this point is to solve (18) and extract an expression for the fine-scale field. This expression can then be substituted in the coarse-scale problem defined by (16) and (17), thereby eliminating the explicit presence of the fine-scales, yet modeling their effect.

Since we are dealing with nonlinear sub-problems, in order to solve the fine-scale problem we need to linearize it. Accordingly, we employ an iterative solution strategy and define the various incremental quantities as follows:

$$\boldsymbol{\sigma}_{n+1}^{i+1} = \boldsymbol{\sigma}_{n+1}^i + \Delta \boldsymbol{\sigma}, \tag{19}$$

$$\boldsymbol{\varepsilon}_{n+1}^{i+1} = \boldsymbol{\varepsilon}_{n+1}^i + \Delta \boldsymbol{\varepsilon}, \tag{20}$$

$$p_{n+1}^{i+1} = p_{n+1}^i + \Delta p, \tag{21}$$

where $(\cdot)_{n+1}^{i+1}$ represents the current iterated value in the current time step of the quantity in the bracket, $(\cdot)_{n+1}^i$ represents the value at the previous iteration in the current time step, while $\Delta(\cdot)$ represents the incremental value between two successive iterates. Substituting the current state of stress $\boldsymbol{\sigma}_{n+1}^{i+1}$ from (19) in (18) and writing it in the residual form we get

$$\int_{\Omega'} \nabla^s \mathbf{w}' : \Delta \boldsymbol{\sigma} \, d\Omega = \int_{\Omega'} \mathbf{w}' \cdot \mathbf{b} \, d\Omega - \int_{\Omega'} \nabla^s \mathbf{w}' : \boldsymbol{\sigma}_{n+1}^i \, d\Omega. \tag{22}$$

As is shown later in Section 5, the linearized incremental stress $\Delta \boldsymbol{\sigma}$ is related to the incremental strain $\Delta \boldsymbol{\varepsilon}$ and incremental pressure Δp via a relation: $\Delta \boldsymbol{\sigma} = \mathbf{D}^{uu} \Delta \boldsymbol{\varepsilon} + \mathbf{D}^{up} \Delta p$. Substituting $\Delta \boldsymbol{\sigma}$ in (22) and employing the definition of the incremental strain, that, because of (13) can be split into the coarse and the fine-scale strain fields, i.e., $\Delta \boldsymbol{\varepsilon} = \Delta \bar{\boldsymbol{\varepsilon}} + \Delta \boldsymbol{\varepsilon}'$, and rearranging the terms we obtain.

$$\int_{\Omega'} \nabla^s \mathbf{w}' : \mathbf{D}^{uu} \Delta \boldsymbol{\varepsilon}' \, d\Omega = \int_{\Omega'} \mathbf{w}' \cdot \mathbf{b} \, d\Omega - \int_{\Omega'} \nabla^s \mathbf{w}' : [\boldsymbol{\sigma}_{n+1}^i + \mathbf{D}^{uu} \Delta \bar{\boldsymbol{\varepsilon}} + \mathbf{D}^{up} \Delta p] \, d\Omega. \tag{23}$$

Without loss of generality we assume that the incremental fine-scale displacement field $\Delta \mathbf{u}'$ is represented via bubble functions $\mathbf{N}^{e'}$. Accordingly, the gradient of the fine-scale displacement field is represented in terms of the gradient of the bubble functions as follows:

$$\Delta \mathbf{u}' = \mathbf{N}^{e'} \Delta \mathbf{u}'_e \Rightarrow \nabla^s \Delta \mathbf{u}' = \nabla^s \mathbf{N}^{e'} \Delta \mathbf{u}'_e = \Delta \boldsymbol{\varepsilon}', \tag{24}$$

$$\mathbf{w}' = \mathbf{N}^{e'} \mathbf{w}'_e \Rightarrow \nabla^s \mathbf{w}' = \nabla^s \mathbf{N}^{e'} \mathbf{w}'_e, \tag{25}$$

where $\Delta \boldsymbol{\varepsilon}'$ is the incremental fine-scale strain field. Substituting (24) and (25) in (23) and taking the vectors of constant coefficients out of the integral expression we get

$$\mathbf{w}'_e{}^T \int_{\Omega'} [(\nabla^s \mathbf{N}^{e'})^T \mathbf{D}^{uu} \nabla^s \mathbf{N}^{e'} \, d\Omega] \Delta \mathbf{u}'_e = \mathbf{w}'_e{}^T [\mathbf{R}_{n+1}^i]. \tag{26}$$

We can now extract the coefficients of the fine-scale incremental displacement field as

$$\Rightarrow \Delta \mathbf{u}'_e = \mathbf{K}_1^{-1} \mathbf{R}_{n+1}^i, \quad (27)$$

where

$$\mathbf{K}_1 = \int_{\Omega'} (\nabla^s \mathbf{N}^{e'})^T \mathbf{D}^{uu} \nabla^s \mathbf{N}^{e'} d\Omega, \quad (28)$$

$$\mathbf{R}_{n+1}^i = \int_{\Omega'} \mathbf{w}' \cdot \mathbf{b} d\Omega - \int_{\Omega'} \nabla^s \mathbf{w}' : [\boldsymbol{\sigma}_{n+1}^i + \mathbf{D}^{uu} \Delta \bar{\boldsymbol{\varepsilon}} + \mathbf{D}^{up} \Delta p] d\Omega. \quad (29)$$

The fine-scale incremental displacement field $\Delta \mathbf{u}'$ can now be constructed via recourse to (24).

$$\Delta \mathbf{u}' = \mathbf{N}^{e'} \mathbf{K}_1^{-1} \mathbf{R}_{n+1}^i. \quad (30)$$

3.3. The modified coarse-scale problem

Let us now consider Eq. (16). Substituting the current state of stress $\boldsymbol{\sigma}_{n+1}^{i+1}$ and rearranging the resulting equation in a residual form, we get

$$\int_{\Omega} \nabla^s \bar{\mathbf{w}} : \Delta \boldsymbol{\sigma} d\Omega = \int_{\Omega} \bar{\mathbf{w}} \cdot \mathbf{b} d\Omega + \int_{\Gamma} \bar{\mathbf{w}} \cdot \mathbf{t} d\Gamma - \int_{\Omega} \nabla^s \bar{\mathbf{w}} : \boldsymbol{\sigma}_{n+1}^i d\Omega. \quad (31)$$

Substituting $\Delta \boldsymbol{\sigma} = \mathbf{D}^{uu} \Delta \boldsymbol{\varepsilon} + \mathbf{D}^{up} \Delta p$ in (31), substituting the incremental strain $\Delta \boldsymbol{\varepsilon} = \Delta \bar{\boldsymbol{\varepsilon}} + \Delta \boldsymbol{\varepsilon}'$, and rearranging terms, we get

$$\int_{\Omega} \nabla^s \bar{\mathbf{w}} : \mathbf{D}^{uu} \Delta \bar{\boldsymbol{\varepsilon}} d\Omega + \int_{\Omega} \nabla^s \bar{\mathbf{w}} : \mathbf{D}^{up} \Delta p d\Omega + \int_{\Omega} \nabla^s \bar{\mathbf{w}} : \mathbf{D}^{uu} \Delta \boldsymbol{\varepsilon}' d\Omega = \int_{\Omega} \bar{\mathbf{w}} \cdot \mathbf{b} d\Omega + \int_{\Gamma} \bar{\mathbf{w}} \cdot \mathbf{t} d\Gamma - \int_{\Omega} \nabla^s \bar{\mathbf{w}} : \boldsymbol{\sigma}_{n+1}^i d\Omega. \quad (32)$$

$\Delta \boldsymbol{\varepsilon}'$ is the gradient of the fine-scale incremental displacement field. Substituting $\Delta \boldsymbol{\varepsilon}' = \nabla^s \Delta \mathbf{u}'$ in (32), then substituting \mathbf{K}_1^{-1} from (28) and \mathbf{R}_{n+1}^i from (29), and rearranging terms we get

$$\begin{aligned} & \int_{\Omega} \nabla^s \bar{\mathbf{w}} : \mathbf{D}^{uu} \Delta \bar{\boldsymbol{\varepsilon}} d\Omega + \int_{\Omega} \nabla^s \bar{\mathbf{w}} : \mathbf{D}^{up} \Delta p d\Omega - \int_{\Omega} \nabla^s \bar{\mathbf{w}} : \mathbf{D}^{uu} \boldsymbol{\tau}_1 [(\mathbf{D}^{uu} \Delta \bar{\boldsymbol{\varepsilon}} + \mathbf{D}^{up} \Delta p)] d\Omega \\ & = \int_{\Omega} \bar{\mathbf{w}} \cdot \mathbf{b} d\Omega + \int_{\Gamma} \bar{\mathbf{w}} \cdot \mathbf{t} d\Gamma - \int_{\Omega} \nabla^s \bar{\mathbf{w}} : (\mathbf{1} - \mathbf{D}^{uu} \boldsymbol{\tau}_1) \boldsymbol{\sigma}_{n+1}^i d\Omega - \int_{\Omega} \nabla^s \bar{\mathbf{w}} : \mathbf{D}^{uu} \boldsymbol{\tau}_2 \mathbf{b} d\Omega, \end{aligned} \quad (33)$$

where

$$\boldsymbol{\tau}_1 = \left(\nabla^s \mathbf{N}^{e'} \int_{\Omega} \nabla^s \mathbf{N}^{e'} d\Omega \right) \left[\int_{\Omega} (\nabla^s \mathbf{N}^{e'})^T \mathbf{D}^{uu} \nabla^s \mathbf{N}^{e'} d\Omega \right]^{-1}, \quad (34)$$

$$\boldsymbol{\tau}_2 = \left(\nabla^s \mathbf{N}^{e'} \int_{\Omega} \mathbf{N}^{e'} d\Omega \right) \left[\int_{\Omega} (\nabla^s \mathbf{N}^{e'})^T \mathbf{D}^{uu} \nabla^s \mathbf{N}^{e'} d\Omega \right]^{-1}. \quad (35)$$

Remark 2. In this derivation of the multiscale/stabilized formulation, the definition of the stability tensors has appeared automatically.

Remark 3. The definition of the stability tensor $\boldsymbol{\tau}_1$ yields a diagonal matrix only for the case of quadrilateral elements in their rectangular configurations (wherein the interior angles are 90° each).

Remark 4. The stability tensor $\boldsymbol{\tau}_1$ yields a full matrix for the case of triangles as well as for the distorted quadrilateral elements. This feature activates the cross-coupling effects in the additional stabilization terms. This cross-coupling effect in the stabilization terms is not present in the GLS or the SUPG methods.

Remark 5. It is important to note that bubble functions reside completely in the definition of the stability tensors. Consequently, the choice of a specific bubble only affects the values of the components in the stability tensors.

Remark 6. The definition of the stability tensor $\boldsymbol{\tau}_1$ is an outcome of the solution of the fine-scale problem, which, because of the assumption that $p' = 0$, is a function of the fine-scale displacement field alone. This feature of the stability parameter helps enriching the displacement field and is therefore attractive from the view point of the ratio of constraint count, i.e., the ratio of the displacement to the pressure degrees of freedom (see [10]).

3.4. The constitutive equation for the pressure field

The weak form of the constraint equation for the pressure field is given by (17). Employing an iterative solution scheme, (17) can be written as

$$\int_{\Omega} q(\boldsymbol{\varepsilon}_{n+1}^{i+1} - \boldsymbol{\varepsilon}_{n+1}^{I,i+1}) \cdot \boldsymbol{\delta} \, d\Omega - \int_{\Omega} q \frac{p_{n+1}^{i+1}}{K} \, d\Omega = 0. \tag{36}$$

Substituting the current iterated values of $\boldsymbol{\varepsilon}_{n+1}^{i+1}$, $\boldsymbol{\varepsilon}_{n+1}^{I,i+1}$ and p_{n+1}^{i+1} in terms of the incremental values leads to the following form:

$$\int_{\Omega} q(\Delta\boldsymbol{\varepsilon} - \Delta\boldsymbol{\varepsilon}^I) \cdot \boldsymbol{\delta} \, d\Omega - \int_{\Omega} q \frac{\Delta p}{K} \, d\Omega = - \int_{\Omega} q \left[(\boldsymbol{\varepsilon}_{n+1}^i - \boldsymbol{\varepsilon}_{n+1}^{I,i}) \cdot \boldsymbol{\delta} - \frac{p_{n+1}^i}{K} \right] \, d\Omega, \tag{37}$$

where $\Delta(\cdot)$ represents the incremental value between two successive iterations. For the J_2 flow theory the volumetric part of the inelastic strain is zero. Consequently (37) simplifies as follows:

$$\int_{\Omega} q \mathbf{D}^{pu} \Delta\boldsymbol{\varepsilon} \, d\Omega - \int_{\Omega} q D^{pp} \Delta p \, d\Omega = - \int_{\Omega} q \left[\boldsymbol{\varepsilon}_{n+1}^i \cdot \boldsymbol{\delta} - \frac{p_{n+1}^i}{K} \right] \, d\Omega, \tag{38}$$

where

$$\mathbf{D}^{pu} = \boldsymbol{\delta} = \mathbf{1}^T, \tag{39}$$

$$D^{pp} = \frac{1}{K}. \tag{40}$$

We now substitute the definition of the incremental strain $\Delta\boldsymbol{\varepsilon} = \Delta\bar{\boldsymbol{\varepsilon}} + \Delta\boldsymbol{\varepsilon}'$ in (38) and rearrange the terms.

$$\int_{\Omega} q \mathbf{D}^{pu} \Delta\bar{\boldsymbol{\varepsilon}} \, d\Omega + \int_{\Omega} q \mathbf{D}^{pu} \Delta\boldsymbol{\varepsilon}' \, d\Omega - \int_{\Omega} q D^{pp} \Delta p \, d\Omega = - \int_{\Omega} q [\mathbf{D}^{pu} \boldsymbol{\varepsilon}_{n+1}^i - D^{pp} p_{n+1}^i] \, d\Omega. \tag{41}$$

Substituting $\Delta\boldsymbol{\varepsilon}'$ in (38) we get

$$\begin{aligned} & \int_{\Omega} q \mathbf{D}^{pu} \Delta\bar{\boldsymbol{\varepsilon}} \, d\Omega - \int_{\Omega} q D^{pp} \Delta p \, d\Omega - \int_{\Omega} q \mathbf{D}^{pu} : \boldsymbol{\tau}_1 [(\mathbf{D}^{uu} \Delta\bar{\boldsymbol{\varepsilon}} + \mathbf{D}^{up} \Delta p)] \, d\Omega \\ & = - \int_{\Omega} q [\mathbf{D}^{pu} \boldsymbol{\varepsilon}_{n+1}^i - D^{pp} p_{n+1}^i] \, d\Omega + \int_{\Omega} q \mathbf{D}^{pu} : [\boldsymbol{\tau}_1 \boldsymbol{\sigma}_{n+1}^i - \boldsymbol{\tau}_2 \mathbf{b}] \, d\Omega. \end{aligned} \tag{42}$$

3.5. The HVM formulation

We can write the linearized form of the HVM stabilized formulation from (33) and (42).

$$\begin{aligned} & \int_{\Omega} \nabla^s \bar{\mathbf{w}} : \mathbf{D}^{uu} \Delta\bar{\boldsymbol{\varepsilon}} \, d\Omega + \int_{\Omega} \nabla^s \bar{\mathbf{w}} : \mathbf{D}^{up} \Delta p \, d\Omega + \int_{\Omega} q \mathbf{D}^{pu} \Delta\bar{\boldsymbol{\varepsilon}} \, d\Omega - \int_{\Omega} q D^{pp} \Delta p \, d\Omega - \int_{\Omega} (\nabla^s \bar{\mathbf{w}} : \mathbf{D}^{uu} + q \mathbf{D}^{pu}) : \boldsymbol{\tau}_1 (\mathbf{D}^{uu} \Delta\bar{\boldsymbol{\varepsilon}} + \mathbf{D}^{up} \Delta p) \, d\Omega \\ & = \int_{\Omega} \bar{\mathbf{w}} \cdot \mathbf{b} \, d\Omega + \int_{\Gamma} \bar{\mathbf{w}} \cdot \mathbf{t} \, d\Gamma - \int_{\Omega} \nabla^s \bar{\mathbf{w}} : \boldsymbol{\sigma}_{n+1}^i \, d\Omega - \int_{\Omega} q [\mathbf{D}^{pu} \boldsymbol{\varepsilon}_{n+1}^i - D^{pp} p_{n+1}^i] \, d\Omega - \int_{\Omega} (\nabla^s \bar{\mathbf{w}} : \mathbf{D}^{uu} + q \mathbf{D}^{pu}) : [-\boldsymbol{\tau}_1 \boldsymbol{\sigma}_{n+1}^i + \boldsymbol{\tau}_2 \mathbf{b}] \, d\Omega, \end{aligned} \tag{43}$$

where $\nabla^s(\cdot)$ represents the symmetric gradient operator, $(\cdot)_{n+1}^i$ represents the value at the previous iteration in the current time step, $\Delta(\cdot)$ represents the incremental value between two successive iterates, while $\boldsymbol{\tau}_1$ and $\boldsymbol{\tau}_2$ are given in (34) and (35), respectively.

Remark 7. It is important to note that (43) is represented completely in terms of the coarse-scale fields. The additional stabilization terms have appeared because of the assumption of the existence of fine-scale displacement field. In (43) these terms are modeling the effects of the residual of coarse-scales over the sum of element interiors.

Remark 8. Since the fine-scale problem is driven by the residual of the coarse scales (23), these terms are based on the residual of the corresponding Euler–Lagrange equations. As such, the proposed formulation yields a consistent method.

3.6. The matrix form of the HVM formulation

We write the matrix equations of the HVM stabilized formulation in the residual form as follows:

$$\begin{bmatrix} \mathbf{K}_1 - \mathbf{K}_6^T \mathbf{K}_5^{-1} \mathbf{K}_6 & \mathbf{K}_2 - \mathbf{K}_6^T \mathbf{K}_5^{-1} \mathbf{K}_7 \\ \mathbf{K}_3 - \mathbf{K}_7^T \mathbf{K}_5^{-1} \mathbf{K}_6 & \mathbf{K}_4 - \mathbf{K}_7^T \mathbf{K}_5^{-1} \mathbf{K}_7 \end{bmatrix} \begin{Bmatrix} \Delta \bar{\mathbf{u}} \\ \Delta p \end{Bmatrix} = \begin{Bmatrix} \mathbf{R}_2 - \mathbf{K}_6^T \mathbf{K}_5^{-1} \mathbf{R}_1 \\ \mathbf{R}_3 - \mathbf{K}_7^T \mathbf{K}_5^{-1} \mathbf{R}_1 \end{Bmatrix}. \quad (44)$$

Although the matrix form (44) is expressed entirely in terms of the coarse-scale displacement and pressure fields, the effects of the subgrid scales are fully represented in the model.

Let $\bar{\mathbf{N}}$ represent the standard interpolation functions for the coarse-scale displacement field, and \mathbf{N}^p represent the interpolation functions for the pressure field. The fine-scale displacement field is represented by \mathbf{N}' , as defined in (24). The various matrices in (44) are as follows:

$$\mathbf{K}_1 = \int_{\Omega} \nabla^{sT} \bar{\mathbf{N}} \mathbf{D}^{uu} \nabla^s \bar{\mathbf{N}} \, d\Omega, \quad (45)$$

$$\mathbf{K}_2 = \int_{\Omega} \nabla^{sT} \bar{\mathbf{N}} \mathbf{D}^{up} \mathbf{N}^p \, d\Omega, \quad (46)$$

$$\mathbf{K}_3 = \int_{\Omega} (\mathbf{N}^p)^T \mathbf{D}^{pu} \nabla^s \bar{\mathbf{N}} \, d\Omega, \quad (47)$$

$$\mathbf{K}_4 = - \int_{\Omega} (\mathbf{N}^p)^T \mathbf{D}^{pp} \mathbf{N}^p \, d\Omega, \quad (48)$$

$$\mathbf{K}_5 = \int_{\Omega} \nabla^{sT} \mathbf{N}' \mathbf{D}^{uu} \nabla^s \mathbf{N}' \, d\Omega, \quad (49)$$

$$\mathbf{K}_6 = \int_{\Omega} \nabla^{sT} \mathbf{N}' \mathbf{D}^{uu} \nabla^s \bar{\mathbf{N}} \, d\Omega, \quad (50)$$

$$\mathbf{K}_7 = \int_{\Omega} \nabla^{sT} \mathbf{N}' \mathbf{D}^{up} \mathbf{N}^p \, d\Omega. \quad (51)$$

$$\mathbf{R}_1 = \int_{\Omega} \mathbf{N}' \cdot \mathbf{b} \, d\Omega - \int_{\Omega} \nabla^s \mathbf{N}' \sigma_{n+1}^i \, d\Omega, \quad (52)$$

$$\mathbf{R}_2 = \int_{\Omega} \bar{\mathbf{N}} \cdot \mathbf{b} \, d\Omega + \int_{\Gamma} \bar{\mathbf{N}} \cdot \mathbf{t} \, d\Gamma - \int_{\Omega} \nabla^s \bar{\mathbf{N}} \sigma_{n+1}^i \, d\Omega, \quad (53)$$

$$\mathbf{R}_3 = - \int_{\Omega} (\mathbf{N}^p)^T [\mathbf{D}^{pu} \boldsymbol{\epsilon}_{n+1}^i - \mathbf{D}^{pp} p_{n+1}^i] \, d\Omega. \quad (54)$$

Remark 9. For the J_2 flow theory, (44) results in a symmetric tangent matrix.

Remark 10. For the case of a linear constitutive equation, the expressions for \mathbf{D}^{uu} , \mathbf{D}^{up} , \mathbf{D}^{pu} and \mathbf{D}^{pp} can be simplified to $\mathbf{D}^{uu} = 2G\mathbf{I}_{\text{dev}}$, $\mathbf{D}^{up} = \mathbf{1}$, $\mathbf{D}^{pu} = \mathbf{1}^T$ and $\mathbf{D}^{pp} = \frac{1}{K}$. In this case the formulation simplifies to that of a stabilized formulation for incompressible elasticity, first presented in [24].

4. A kinetic cosine model for superelasticity

This section presents a 3D nonlinear kinetic cosine model for superelasticity in SMAs under mechanical loading/unloading conditions at constant high temperature. Shape memory alloys usually present thermoelastic martensitic transformations, however in this paper we limit the model to the pseudo-elastic behavior of SMAs [23]. We assume that the transformations are a function of the deviatoric part s of the stress tensor $\boldsymbol{\sigma}$. We therefore generalize the concept of uniaxial stress range using a J_2 -type norm indicated by S , where J_2 is the second invariant of the deviatoric part of stress.

$$S = \|\mathbf{s}\| = \sqrt{s_{ij} : s_{ij}} = \sqrt{2J_2}. \quad (55)$$

Fig. 1 describes the kinetics of phase transformations for the complete phase change from Martensite to Austenite ($M \rightarrow A$), from Austenite to Martensite ($A \rightarrow M$), and also the incomplete transformations between these two phases.

For complete phase transformation between austenite and martensite, we first define the stress range for the activation of transformation.

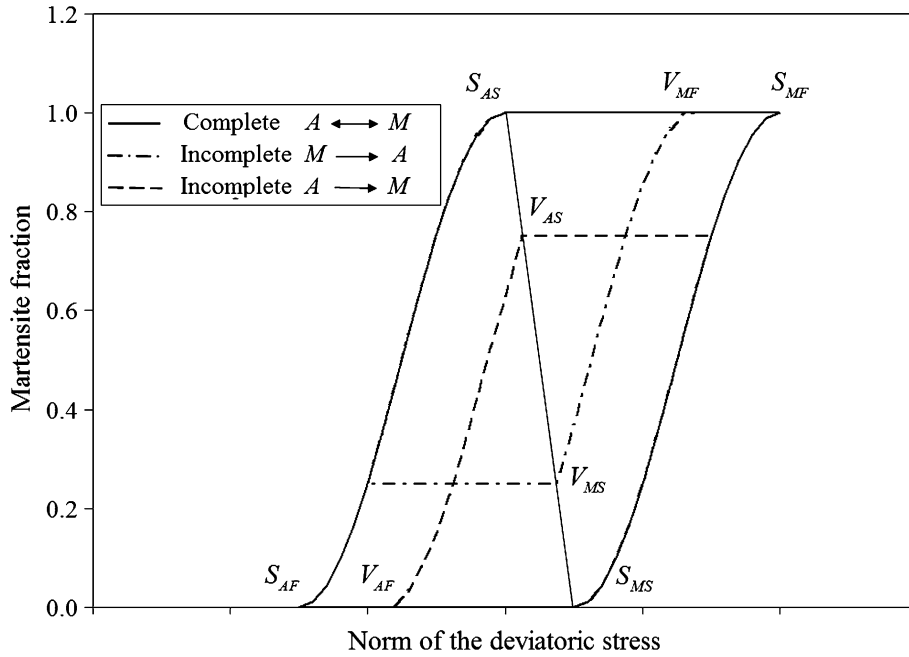


Fig. 1. Schematic diagram of the constitutive model.

$$S_{MS} \leq S \leq S_{MF}, \quad \dot{S} > 0 \Rightarrow (A \rightarrow M), \tag{56}$$

$$S_{AF} \leq S \leq S_{AS}, \quad \dot{S} < 0 \Rightarrow (M \rightarrow A), \tag{57}$$

where S_{MS} and S_{MF} represent the norms of the martensite-start and martensite-finish deviatoric stresses, respectively. Likewise, S_{AS} and S_{AF} represent the norms of the austenite-start and austenite-finish deviatoric stresses, respectively. The three dimensional S bounds, i.e., S_{MS} , S_{MF} , S_{AS} and S_{AF} are related to the experimentally obtained uniaxial σ bounds through the J_2 -type norm (55).

The phase transformation functions or the yield functions for $A \rightarrow M$ and $M \rightarrow A$ transformations are given by $F_{AM}(\xi, S)$ and $F_{MA}(\xi, S)$, respectively.

$$F_{AM}(\xi, S) = \xi - \frac{1}{2} \cos[a_M(S - V_{MF})] - \frac{1}{2}(V_{MS} \leq S \leq V_{MF}), \tag{58}$$

$$F_{MA}(\xi, S) = \xi + \frac{1}{2} \cos[a_A(S - V_{AF})] - \frac{1}{2}(V_{AF} \leq S \leq V_{AS}), \tag{59}$$

where ξ is a scalar internal variable that represents the martensite fraction.

The evolution of the martensite fraction ξ for complete phase transformation is given by

$$\xi = \begin{cases} \frac{1}{2} \{ \cos[a_M(S - S_{MF})] + 1 \} & (A \rightarrow M), \\ \frac{1}{2} \{ -\cos[a_A(S - S_{AF})] + 1 \} & (M \rightarrow A), \end{cases} \tag{60}$$

where $a_M = \frac{\pi}{(S_{MS} - S_{MF})}$ and $a_A = \frac{\pi}{(S_{AS} - S_{AF})}$.

For partial phase transformations from austenite to martensite ($A \rightarrow M$), the martensite fraction is given by

$$\xi = \frac{1}{2} \{ \cos[a_M(S - V_{MF})] + 1 \} \quad (V_{MS} \leq S \leq V_{MF}). \tag{61}$$

The limiting stresses for the start and the finish of the partial $A \rightarrow M$ transformations are given by

$$V_{MS} = (1 - \xi_p)S_{MS} + \xi_p S_{AS}, \tag{62}$$

$$V_{MF} = (1 + \xi_p)S_{AS} + (1 - \xi_p)S_{MS} - S_{AF} - \frac{\arccos(1 - 2\xi_p)}{a_A}, \tag{63}$$

where ξ_p is the value of ξ in the previous reverse transformation. Similarly, for the partial phase transformations from martensite to austenite ($M \rightarrow A$), the martensite fraction is given by

$$\xi = \frac{1}{2} \{ -\cos[a_A(S - V_{AF})] + 1 \} \quad (V_{AF} \leq S \leq V_{AS}). \tag{64}$$

The limiting stresses that control the partial $M \rightarrow A$ transformations are given by

$$V_{AS} = (1 - \xi_p)S_{MS} + \xi_p S_{AS}, \quad (65)$$

$$V_{AF} = (2 - \xi_p)S_{MS} - S_{MF} + \xi_p S_{AS} - \frac{\arccos(2\xi_p - 1)}{a_M}. \quad (66)$$

We append the Kuhn–Tucker type two-way phase transformation conditions to the model.

$$\dot{\xi} \geq 0, \quad F_{AM}(S, \xi) \leq 0, \quad \dot{\xi} F_{AM}(S, \xi) = 0 \quad (A \rightarrow M), \quad (67)$$

$$\dot{\xi} \leq 0, \quad F_{MA}(S, \xi) \geq 0, \quad \dot{\xi} F_{MA}(S, \xi) = 0 \quad (M \rightarrow A). \quad (68)$$

Eq. (67) represents the Kuhn–Tucker constraint on the admissible state of stress for austenite to martensite conversion that takes place during loading, i.e., $\dot{S} > 0$. Likewise, Eq. (68) represents the Kuhn–Tucker constraint for martensite to austenite conversion that takes place during unloading, i.e., $\dot{S} < 0$.

The consistency conditions for loading ($A \rightarrow M$) and unloading ($M \rightarrow A$) are given as follows:

$$\dot{\xi} \dot{F}_{AM}(S, \xi) = 0 \quad (A \rightarrow M), \quad (69)$$

$$\dot{\xi} \dot{F}_{MA}(S, \xi) = 0 \quad (M \rightarrow A). \quad (70)$$

5. Constitutive integration algorithm

Employing ideas from elastoplasticity [29], in this section we present a constitutive integration algorithm for the super-elastic behavior of SMAs. We consider an additive decomposition of the nonlinear strain tensor into elastic and inelastic parts

$$\boldsymbol{\varepsilon} = \boldsymbol{\varepsilon}^E + \boldsymbol{\varepsilon}^I. \quad (71)$$

We assume that the volumetric change due to inelastic strain is zero, $\text{tr} \boldsymbol{\varepsilon}^I = 0$, and that superelasticity or the phase change behavior is a function of only the deviatoric part of the inelastic strains.

We write the stress tensor as

$$\boldsymbol{\sigma} = \boldsymbol{s} + p\mathbf{1}, \quad (72)$$

where \boldsymbol{s} is the deviatoric stress, and p is the volumetric-stress or the hydrostatic pressure in the incompressible limit. In the mixed displacement–pressure formulation, pressure p is considered to be an independent field. The deviatoric stress is related to the deviatoric projection of the strain field. The elastic deviatoric stress can be written as

$$\boldsymbol{s} = 2G(\boldsymbol{e} - \boldsymbol{e}^I), \quad (73)$$

where $\boldsymbol{e} = \mathbf{I}_{\text{dev}} \boldsymbol{\varepsilon}$ is the deviatoric strain, and $\mathbf{I}_{\text{dev}} = \mathbf{I} - \frac{1}{3} \mathbf{1} \otimes \mathbf{1}$ is the deviatoric projection operator. \boldsymbol{e}^I is the deviatoric inelastic strain defined by $\boldsymbol{e}^I = \boldsymbol{e}_L^T \boldsymbol{x}$. Accordingly, the evolution equation for the inelastic deviatoric strain is as follows.

$$\dot{\boldsymbol{e}}^I = \boldsymbol{e}_L^T \dot{\boldsymbol{x}}, \quad (74)$$

where \boldsymbol{e}_L^T is a material parameter, obtained experimentally and is related to the so-called maximum residual strain under uniaxial state commonly represented as $\boldsymbol{\varepsilon}_L$, i.e.,

$$\boldsymbol{e}_L^T = \sqrt{\frac{3}{2}} \boldsymbol{\varepsilon}_L. \quad (75)$$

The evolution equation for $\dot{\boldsymbol{x}}$ is assumed to be of the form

$$\dot{\boldsymbol{x}} = \dot{\xi} \boldsymbol{n}, \quad (76)$$

where $\boldsymbol{n} = \frac{\boldsymbol{s}}{\|\boldsymbol{s}\|}$ is the unit vector normal to the phase transformation surface.

Applying an implicit integration scheme for the inelastic strains, the constitutive equation can be expressed at step $(n + 1)$ as

$$\boldsymbol{\sigma}_{n+1} = \boldsymbol{s}_{n+1} + p_{n+1} \mathbf{1} = 2G(\boldsymbol{e}_{n+1} - \boldsymbol{e}_{n+1}^I) + p_{n+1} \mathbf{1}, \quad (77)$$

where \boldsymbol{e}_{n+1}^I is obtained as follows:

$$\boldsymbol{e}_{n+1}^I = \boldsymbol{e}_n^I + \boldsymbol{e}_L^T \dot{\xi} \Delta t \boldsymbol{n} = \boldsymbol{e}_n^I + \boldsymbol{e}_L^T \lambda \boldsymbol{n} = \boldsymbol{e}_n^I + \Delta \boldsymbol{e}^I. \quad (78)$$

In (78), λ is the consistency parameter that is obtained by applying the Kuhn–Tucker constraint to the admissible phase change during loading ($A \rightarrow M$) or unloading ($M \rightarrow A$) [26,29]. The numerical integration technique to evaluate λ is given in Lemma 2.

To solve a nonlinear problem we invariably employ an iterative solution strategy. Consequently, Eq. (77) can be written in an iterative form as:

$$\boldsymbol{\sigma}_{n+1}^{i+1} = 2G(\mathbf{e}_{n+1}^{i+1} - \mathbf{e}_{n+1}^{I,i+1}) + p_{n+1}^{i+1} \mathbf{1}, \tag{79}$$

where \mathbf{e}_{n+1}^{i+1} and $\mathbf{e}_{n+1}^{I,i+1}$ are the total and inelastic deviatoric strains defined as

$$\mathbf{e}_{n+1}^{i+1} = \mathbf{e}_{n+1}^i + \Delta \mathbf{e}, \tag{80}$$

$$\mathbf{e}_{n+1}^{I,i+1} = \mathbf{e}_{n+1}^{I,i} + \Delta \mathbf{e}^I. \tag{81}$$

Substituting (80) and (81) into (79) and rearranging terms one can obtain the following set of equations for the deviatoric stress.

$$\mathbf{s}_{n+1}^i = 2G(\mathbf{e}_{n+1}^i - \mathbf{e}_{n+1}^{I,i}), \tag{82}$$

$$\Delta \mathbf{s} = 2G(\Delta \mathbf{e} - \Delta \mathbf{e}^I). \tag{83}$$

We have assumed that the inelastic deformation is caused only by the deviatoric stress and is independent of the hydrostatic pressure. From (78) one can obtain the incremental inelastic deviatoric strain by linearizing the nonlinear expression for martensite fraction ξ , and by satisfying Kuhn–Tucker type constraint conditions presented in (67) and (68).

$$\Delta \mathbf{e}^I = \mathbf{e}_L^T (\Delta \lambda \mathbf{n} + \lambda \Delta \mathbf{n}) = \mathbf{e}_L^T \left(\Delta \lambda \mathbf{n} + \frac{\lambda}{\|\mathbf{s}\|} \mathbf{N} : \Delta \mathbf{s} \right), \tag{84}$$

where $\mathbf{N} = \mathbf{I} - \mathbf{n} \otimes \mathbf{n}$. $\Delta \lambda$ is the incremental consistency parameter given in Lemma 2.

Substituting (84) in (83) and rearranging terms

$$\left(\mathbf{I} + \frac{2G\mathbf{e}_L^T \lambda}{\|\mathbf{s}\|} \mathbf{N} \right) \Delta \mathbf{s} = 2G\Delta \mathbf{e} - 2G\mathbf{e}_L^T \Delta \lambda \mathbf{n}. \tag{85}$$

Simplifying (85) we get the incremental deviatoric stress

$$\Delta \mathbf{s} = 2G[\mathbf{I} + b\mathbf{N}] : \Delta \mathbf{e} - 2G\mathbf{e}_L^T \Delta \lambda \mathbf{n}, \tag{86}$$

where $b = -2G\mathbf{e}_L^T \lambda / (\|\mathbf{s}\| + 2G\mathbf{e}_L^T \lambda)$, and we have used the identities $\mathbf{N}\mathbf{N} = \mathbf{N}$ and $\mathbf{N}\mathbf{n} = \mathbf{0}$. The incremental stress $\Delta \boldsymbol{\sigma}$ is obtained as follows:

$$\Delta \boldsymbol{\sigma} = \Delta \mathbf{s} + \Delta p \mathbf{1} \tag{87}$$

$$= 2G[\mathbf{I} + b\mathbf{N} - \mathbf{e}_L^T \lambda^* \mathbf{n} \otimes \mathbf{n}] : \mathbf{I}_{\text{dev}} \Delta \boldsymbol{\varepsilon} + \Delta p \mathbf{1} \tag{88}$$

$$= \mathbf{D}^{\text{dev}} \Delta \boldsymbol{\varepsilon} + \mathbf{D}^{\text{up}} \Delta p, \tag{89}$$

where \mathbf{D}^{dev} and \mathbf{D}^{up} are given by

$$\mathbf{D}^{\text{dev}} = 2G[\mathbf{I} + b\mathbf{N} - \mathbf{e}_L^T \lambda^* \mathbf{n} \otimes \mathbf{n}] : \mathbf{I}_{\text{dev}}, \tag{90}$$

$$\mathbf{D}^{\text{up}} = \mathbf{1}. \tag{91}$$

Lemma 1. The unit vector $\mathbf{n} = \frac{\mathbf{s}}{\|\mathbf{s}\|}$ can be linearized as follows:

$$\Delta \mathbf{n} = \frac{1}{\|\mathbf{s}\|} [\mathbf{I} - \mathbf{n} \otimes \mathbf{n}] \Delta \mathbf{s} = \frac{\mathbf{N}}{\|\mathbf{s}\|} : \mathbf{I}_{\text{dev}} : \Delta \boldsymbol{\sigma}. \tag{92}$$

Lemma 2. The consistency parameter λ is obtained by applying local Newton Raphson method to the linearized form of the phase transformation equations given in (58) and (59). Accordingly, $\Delta \lambda$ for the two transformation cases is as follows:

$$\Delta \lambda = \begin{cases} \chi_{AM} \mathbf{n} : \mathbf{I}_{\text{dev}} : \Delta \boldsymbol{\varepsilon} & \text{for } (A \rightarrow M), \\ \chi_{MA} \mathbf{n} : \mathbf{I}_{\text{dev}} : \Delta \boldsymbol{\varepsilon} & \text{for } (M \rightarrow A), \end{cases} \tag{93}$$

where

$$\chi_{AM} = \frac{-\alpha_1}{1 - e_L^T \alpha_1} \quad \text{for } (A \rightarrow M), \tag{94}$$

$$\chi_{MA} = \frac{\alpha_2}{1 + e_L^T \alpha_2} \quad \text{for } (M \rightarrow A) \tag{95}$$

and

$$\alpha_1 = a_M G \sin[a_M (S^{TR} - 2Ge_L^T \lambda - V_{MF})], \tag{96}$$

$$\alpha_2 = a_A G \sin[a_A (S^{TR} - 2Ge_L^T \lambda - V_{AF})]. \tag{97}$$

6. Numerical examples

The objective of this work has been to present a method for systematic development of multiscale/stabilized formulations that accommodate nonlinear constitutive models. This section presents various numerical tests to verify the stability and accuracy properties of the proposed formulation. Fig. 2a shows 2D elements and Fig. 2b shows 3D elements that have been developed based on the formulation presented in Section 5. In Fig. 2a and b dots correspond to the displacement nodes and circles correspond to the pressure nodes. The following quadrature rules were used throughout: 3-node triangle, 4-point Gauss quadrature; 4-node quadrilateral, 2 × 2 Gauss quadrature; brick element, 2 × 2 × 2 Gauss quadrature; and tetrahedral element, 4-point Gauss quadrature; (see Hughes [10], Chapter 3). We have employed the simplest polynomial bubbles in all the element types, which in the element natural coordinate frame are expressed as follows:

In 2D:

$$N(\xi, \eta)_{\text{quads}} = (1 - \xi^2)(1 - \eta^2), \tag{98}$$

$$N(\xi, \eta)_{\text{triangles}} = 27\xi\eta(1 - \xi - \eta). \tag{99}$$

In 3D:

$$N(\xi, \eta, \zeta)_{\text{bricks}} = (1 - \xi^2)(1 - \eta^2)(1 - \zeta^2), \tag{100}$$

$$N(\xi, \eta, \zeta)_{\text{tetrahedra}} = 256\xi\eta\zeta(1 - \xi - \eta - \zeta). \tag{101}$$

6.1. Rate of convergence study

It is important to note that if we employ a linear material model in the proposed framework, we recover the stabilized form for nearly-incompressible elasticity presented in Masud and Xia [24]. In this section we use the numerical rate of convergence study to establish that the proposed formulation gives rise to convergent elements. Accordingly, we present the numerically evaluated rates of convergence for the displacement field in the energy norm, and for the pressure field in the $L_2(\Omega)$ norm. The exact solution depends on Poisson’s ratio; the value 0.4999 is employed in the calculations to model the nearly incompressible behavior of the material. In the present study, plane strain conditions are assumed in force. A cantilever beam of length-to-depth ratio equal to five is subjected to a parabolically varying end load. Boundary conditions are set in accordance with an exact elasticity solution. This is a standard problem that is employed to assess the performance of plane stress/strain elements subjected to dominant in-plane bending behavior. The meshes employed consisted

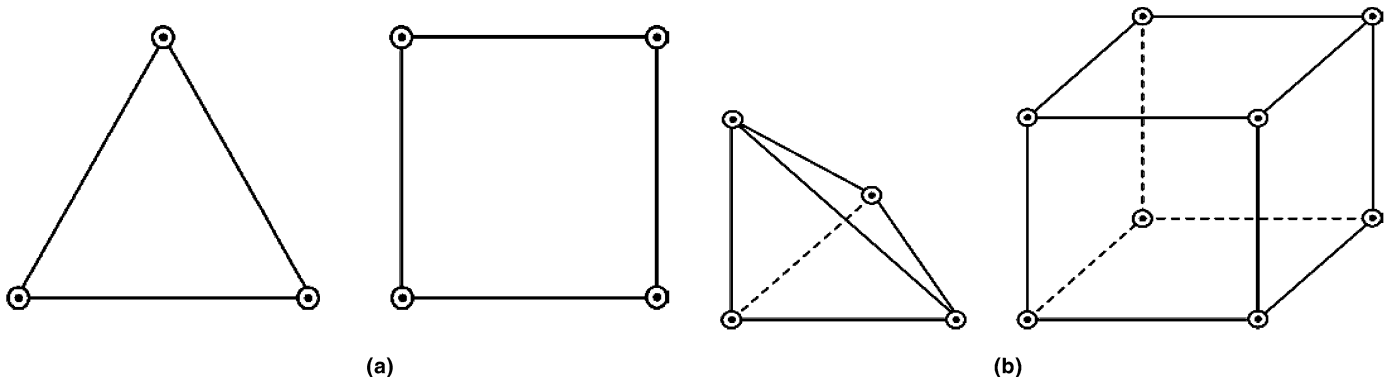


Fig. 2. (a) 2-D elements and (b) 3-D elements.

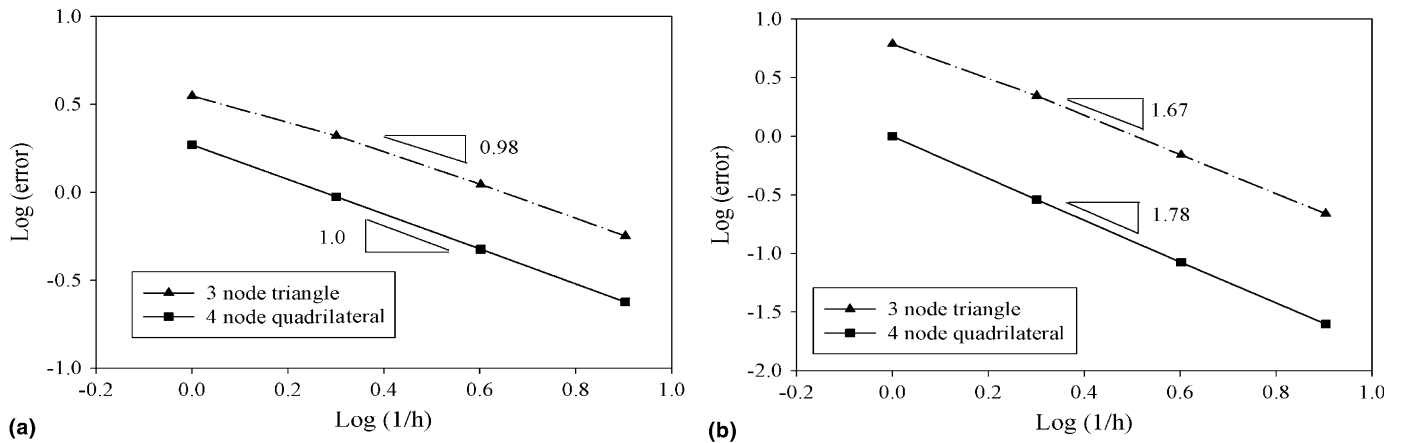


Fig. 3. (a) Convergence rates in the energy norm for the displacement field and (b) convergence rates in the L_2 norm for the pressure field.

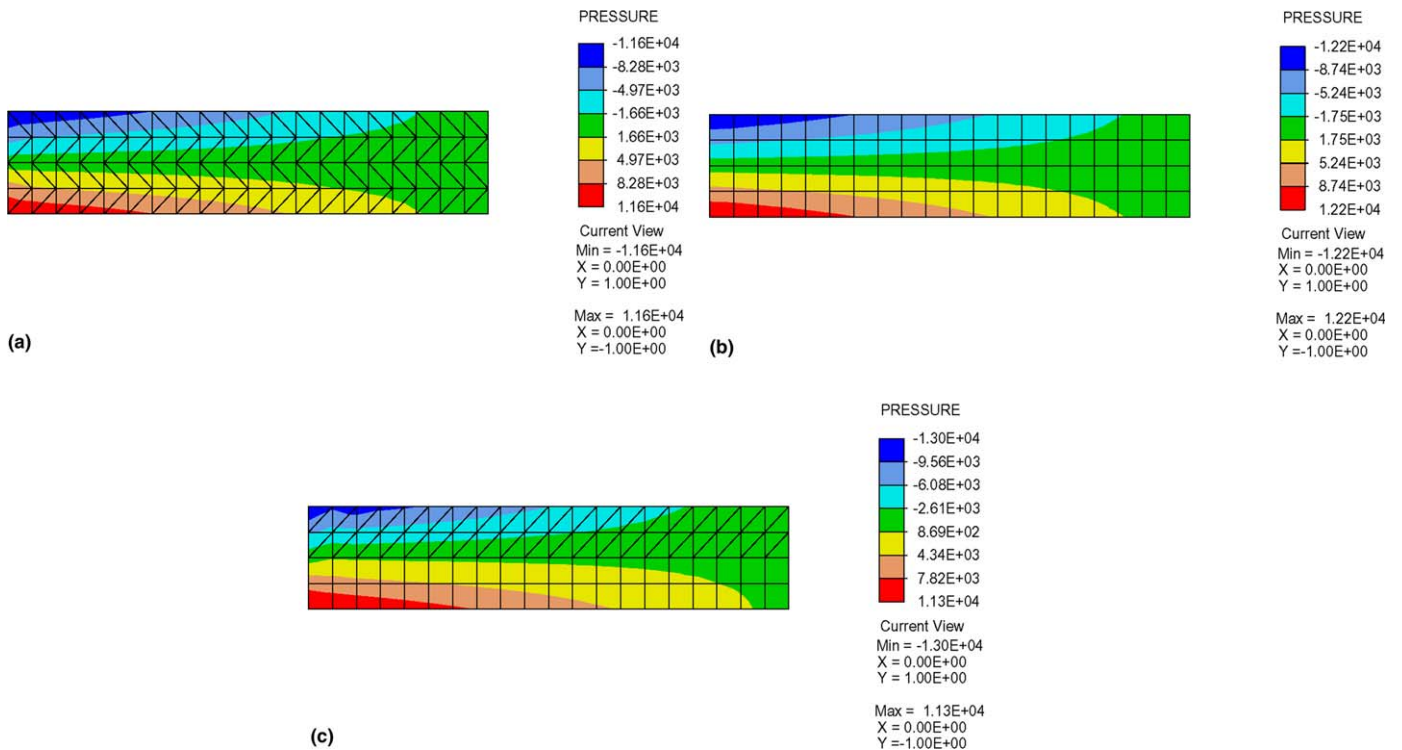


Fig. 4. Contours of the pressure field for (a) the 3-node element mesh, (b) the 4-node element mesh and (c) the composite mesh of linear elements.

of 16 quadrilateral elements in 8×2 format. The meshes for triangles were developed by bisecting the quadrilaterals along the main diagonal. Finer meshes were constructed by uniformly bisecting the parent meshes.

The exact solution to an applied shear force is a third-order polynomial. The two numerical examples show that with successive mesh refinements, the finite element solution converges to the exact solution at nearly the optimal rate for the norms considered. For the 3-node triangle and the 4-node quadrilateral, the theoretical rate of convergence for the displacement field in the energy norm is 1, while the optimal rate for the pressure field in $L_2(\Omega)$ norm is 2. Fig. 3 presents convergence in the energy norm of the displacement field and optimal rates are attained. The convergence in the $L_2(\Omega)$ norm of the pressure field is presented in Fig. 4.

6.2. Test of the incompressibility constraint

With the help of this numerical example we show that the proposed stabilized formulation does not suffer from the locking phenomena, an issue that arises when standard Galerkin methods are used for modeling incompressible materials. In

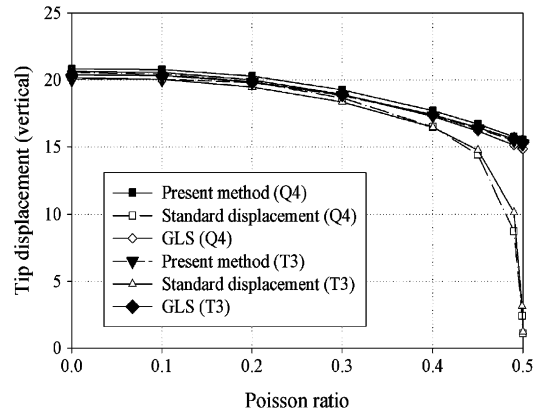


Fig. 5. Tip deflection convergence as a function of Poisson's ratio.

this test case, plain strain conditions are enforced. Fig. 5 presents the vertical displacement at the tip of the cantilever beam (used in the rate of convergence study) as a function of the Poisson's ratio. The elements based on the proposed formulation work all the way to the incompressible limit. A comparison is made with the elements that are based on the Galerkin/Least-squares (GLS) stabilization proposed in Hughes and Franca [14]. It can be seen that the pure displacement-based standard elements show severe locking in the incompressible limit.

6.3. Comparison of the SMA model with the published results

In this section we present the nonlinear response of the constitutive model and compare it with the published results [6]. Fig. 6 exhibits a complete hysteresis loop; the material is austenite prior to loading, transforms to martensite during loading and later completes the reverse transformation to austenite upon unloading. We obtain a good correlation with the kinetic cosine model of Brinson [6] and the kinetic linear model of Masud et al. [23]. (The material properties for this simulation correspond to the ones in [6].)

Next simulation is another complete superelastic loading–unloading of the model at 60 °C and a comparison is made with the cosine model by Brinson and Hwang [7] and the linear model in Masud et al. [23] (see Fig. 7). Brinson's model also compares well with the models presented by Pence and Tanaka (see [7] for a comparative analysis of these models). The material properties used here have been taken from [7].

6.4. Study of 8-node brick element

To further test (i) the stabilized formulation, (ii) the constitutive model, and (iii) the integration algorithm, a series of uniaxial simulations were performed under displacement control. Table 1 presents the material properties employed in the simulations.

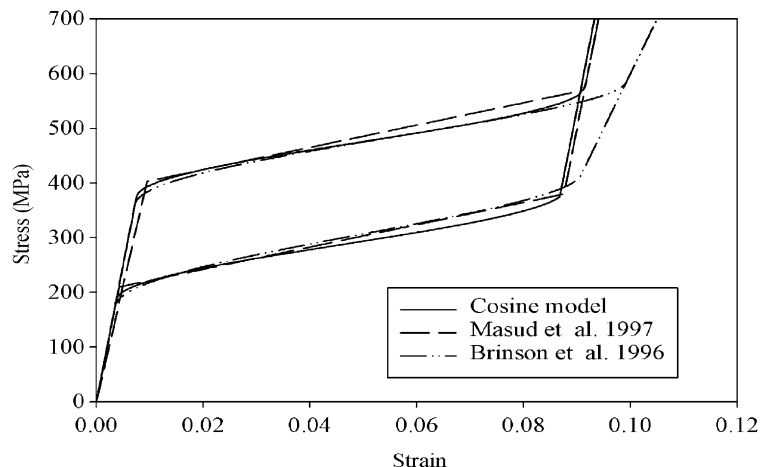


Fig. 6. Comparison of stress vs. strain response for three different constitutive models; unloading from $\xi = 1$.

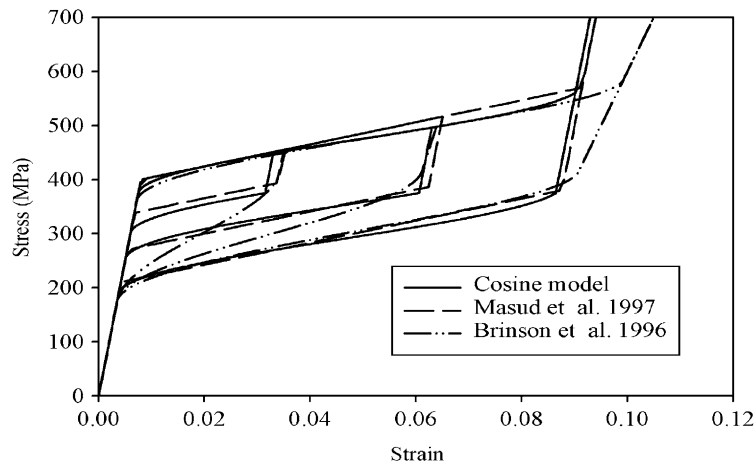


Fig. 7. Comparison of stress vs. strain response for three different constitutive models; unloading from $\xi = 1/3$, $\xi = 2/3$ and $\xi = 1$.

Table 1
Material properties used in the simulation

Young's modulus	E	7500 MPa
Poisson's ratio	ν	0.499
Austenite start stress	S_{AS}	70 MPa
Austenite finish stress	S_{AF}	55 MPa
Martensite start stress	S_{MS}	75 MPa
Martensite finish stress	S_{MF}	90 MPa
Width of the hysteresis loop	e_L^T	0.06

The numerical simulations are organized as follows:

Test 1: Incomplete $A \rightarrow M$ but complete $M \rightarrow A$ transformations

This test presents the numerical response during incomplete $A \rightarrow M$ but complete $M \rightarrow A$ transformation. The strain is increased gradually to various levels followed by unloading of the specimen to zero stress condition in each cycle. Fig. 8a presents the stress–strain plot of the internal loops within the hysteresis loop. Fig. 8b shows the variation in the internal parameter ξ as a function of stress at a typical integration point.

Test 2: Complete $A \rightarrow M$ but incomplete $M \rightarrow A$ transformations

This is a test of complete $A \rightarrow M$ but incomplete $M \rightarrow A$ transformation. The specimen is unloaded to zero stress state only at the end of the final loading cycle. Fig. 9a presents the stress–strain plot with the internal loops representing the metastable states. The variation in ξ as a function of stress is presented in Fig. 9b.

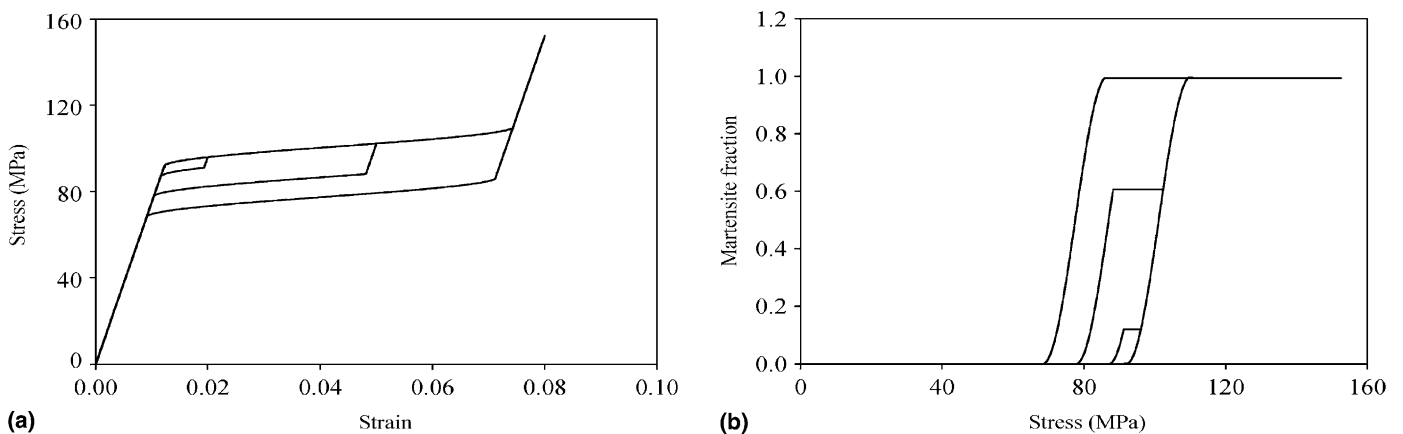


Fig. 8. 8-node brick. (a) Stress vs. strain (incomplete $A \rightarrow M$ but complete $M \rightarrow A$) and (b) internal parameter vs. stress (incomplete $A \rightarrow M$ but complete $M \rightarrow A$).

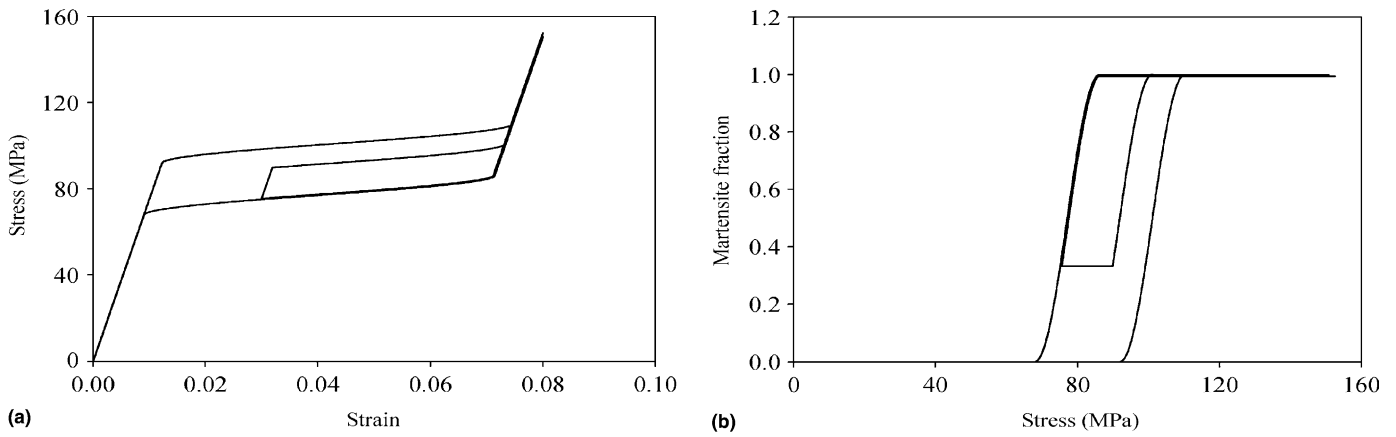


Fig. 9. 8-node brick. (a) Stress vs. strain (complete $A \rightarrow M$ but incomplete $M \rightarrow A$) and (b) internal parameter vs. stress (complete $A \rightarrow M$ but incomplete $M \rightarrow A$).

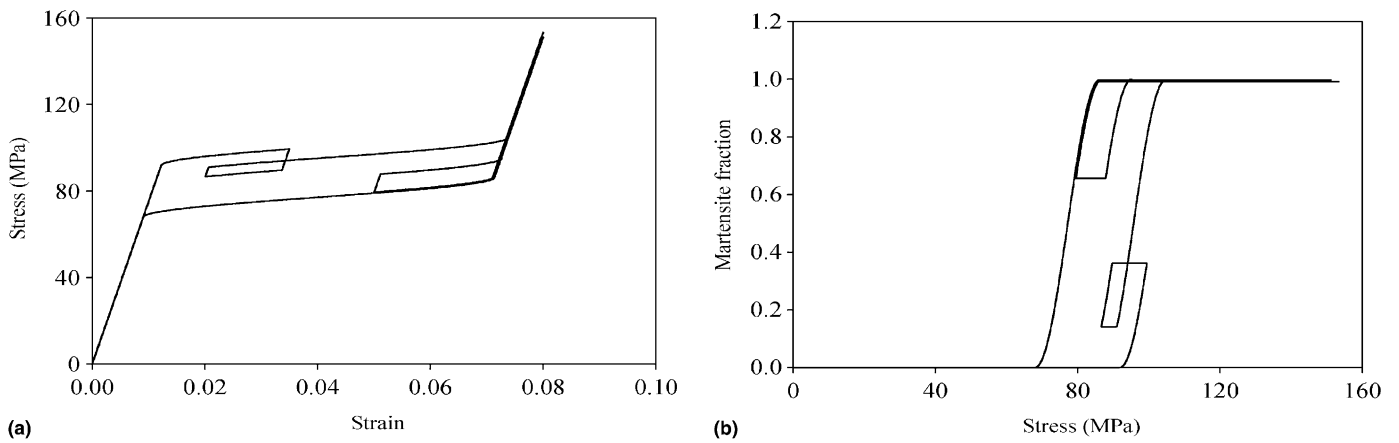


Fig. 10. 8-node brick. (a) Stress vs. strain (incomplete $A \rightarrow M$ and incomplete $M \rightarrow A$) and (b) internal parameter vs. stress (incomplete $A \rightarrow M$ and incomplete $M \rightarrow A$).

Test 3: Incomplete $A \rightarrow M$ and incomplete $M \rightarrow A$ transformations

This test simulates incomplete $A \rightarrow M$ and incomplete $M \rightarrow A$ transformation. A random strain loading is applied as a function of the pseudo-time parameter. The specimen shows *strong path dependence* as presented in Fig. 10a. A similar behavior depicted by the internal parameter ξ is shown in Fig. 10b.

6.5. Study of 4-node tetrahedra element

Figs. 11–13 present the partial phase transformations for the 4-node tetrahedra elements. Once again we see a stable constitutive response for the three different test cases in their entire range of deformation.

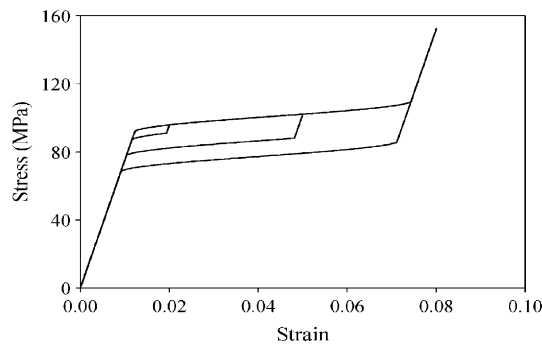


Fig. 11. 4-node tetrahedron. Stress vs. strain (incomplete $A \rightarrow M$ but complete $M \rightarrow A$).

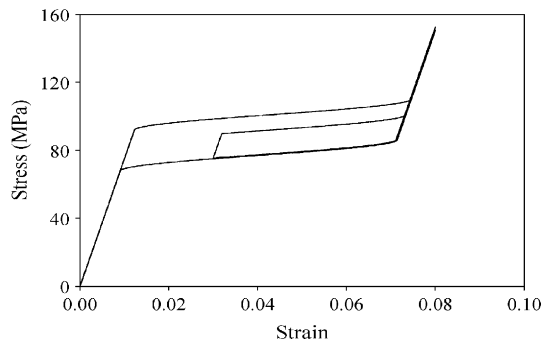


Fig. 12. 4-node tetrahedron. Stress vs. strain (complete $A \rightarrow M$ but incomplete $M \rightarrow A$).

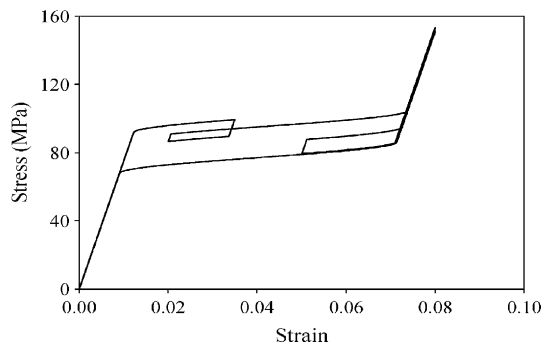


Fig. 13. 4-node tetrahedron. Stress vs. strain (incomplete $A \rightarrow M$ and incomplete $M \rightarrow A$).

6.6. Test of the inelastic incompressibility condition

This numerical simulation is rather of an academic interest to check the performance of the model both in tension and in compression, and to assess the stabilized formulation in terms of its ability to handle inelastic incompressibility. The inelastic incompressibility or the isochoric volumetric constraint becomes more significant in the compression region that is indicated by the lower left quadrant in Fig. 14. The response from the 8-node bricks and the 4-node tetrahedra lies on top of each other and is almost indistinguishable. Once again a stable hysteresis loop is observed in this simulation that indicates that the formulation is free of volumetric locking effects.

6.7. Biaxial bending of a cantilever beam

This numerical simulation shows the load deflection response of a thin-deep cantilever beam when subjected to biaxial loading. The geometry of the beam is $x = 40$ mm, $y = 2$ mm, and $z = 8$ mm. The beam is fixed at one end and driven by an edge shear at the free end. Table 2 presents the material properties employed in the simulations. The shear load

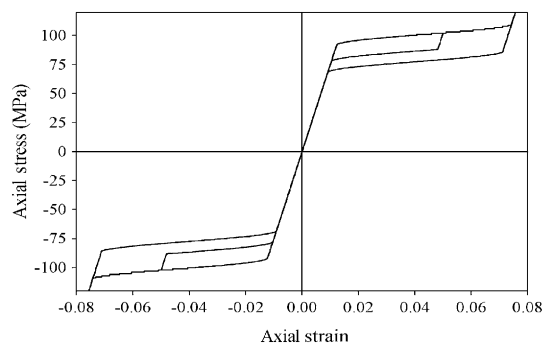


Fig. 14. Hysteresis loops in tension and compression for 8-node bricks and 4-node tetrahedra (incomplete $A \rightarrow M$ but complete $M \rightarrow A$).

Table 2
Material properties used in the simulation

Young's modulus	E	5000 MPa
Poisson's ratio	ν	0.35
Austenite start stress	S_{AS}	100 MPa
Austenite finish stress	S_{AF}	70 MPa
Martensite start stress	S_{MS}	110 MPa
Martensite finish stress	S_{MF}	140 MPa
Width of the hysteresis loop	e_L^T	0.06

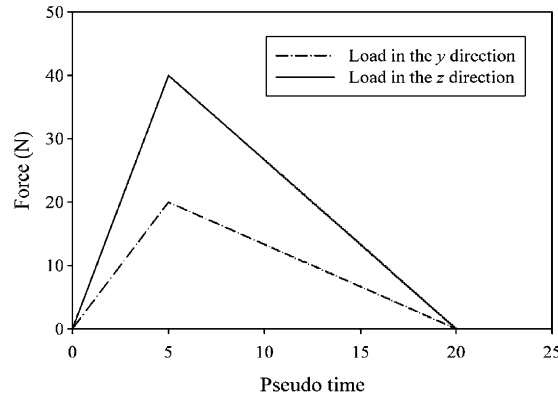


Fig. 15. Load–time history for biaxial bending.

in the transverse and the vertical directions, y and z respectively, is given in Fig. 15. The mesh is composed of 8-node bricks with 16 elements along the length, four elements through the depth and two through the thickness. The mesh for the tetrahedra is made by dividing each of the brick elements into six tetrahedral elements. Two nodal points are selected for the load–displacement diagrams, point B which is at the tip of the beam and point A which is one-eighth the length away from the tip. U_z is the vertical deflection while U_y is the out of plane deflection of the cantilever beam. Fig. 16a and b presents the surface stress distribution of the axial stress for the brick and the tetrahedra elements, respectively. Fig. 17 presents the displacement vs. load–factor response for the 8-node brick elements, and a stable response is attained. The same test is repeated with the 4-node tetrahedra elements. As expected the response of the tetrahedra elements is slightly stiff as compared to that of the brick elements (see Fig. 18a and b), however a stable behavior is observed in the entire range. In both the cases we see hysteresis loops in the load–displacement diagrams that show the multiaxial pseudo-elastic behavior of the SMA model.

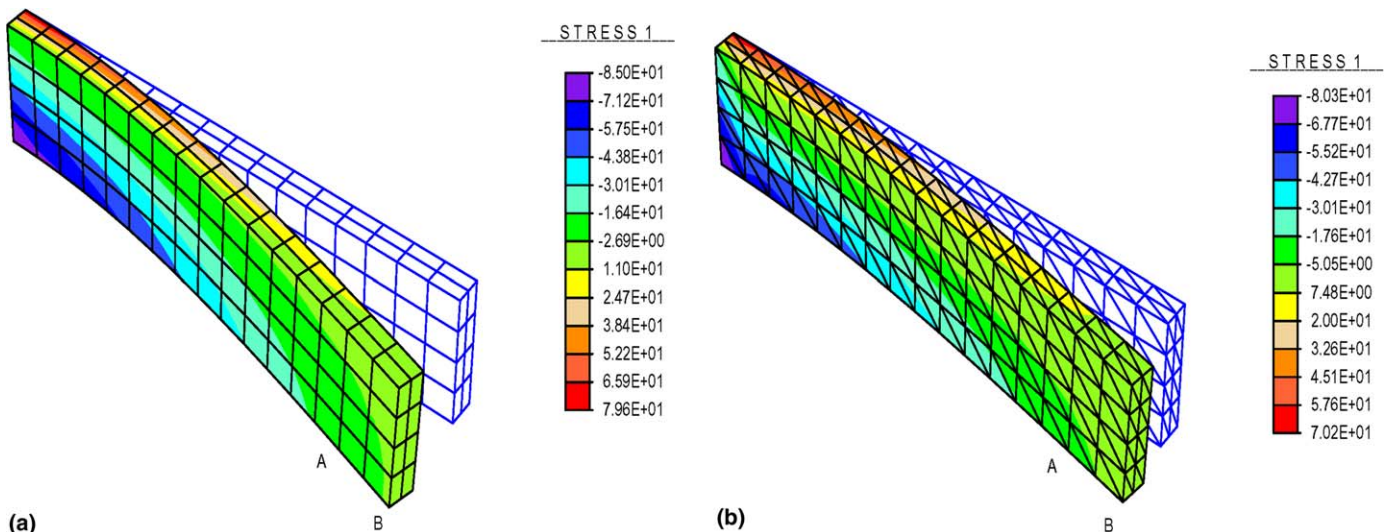


Fig. 16. Axial stress projected on the deformed configuration of (a) the 8-node brick mesh and (b) the 4-node tetrahedra mesh.

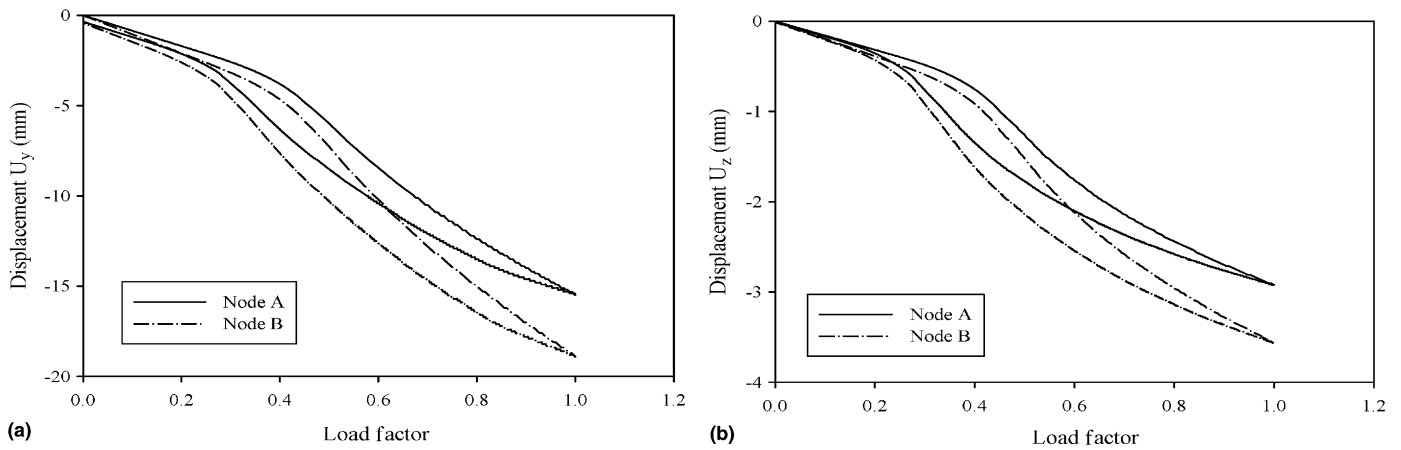


Fig. 17. Load–deflection U_y (a) and U_z (b) for bricks.

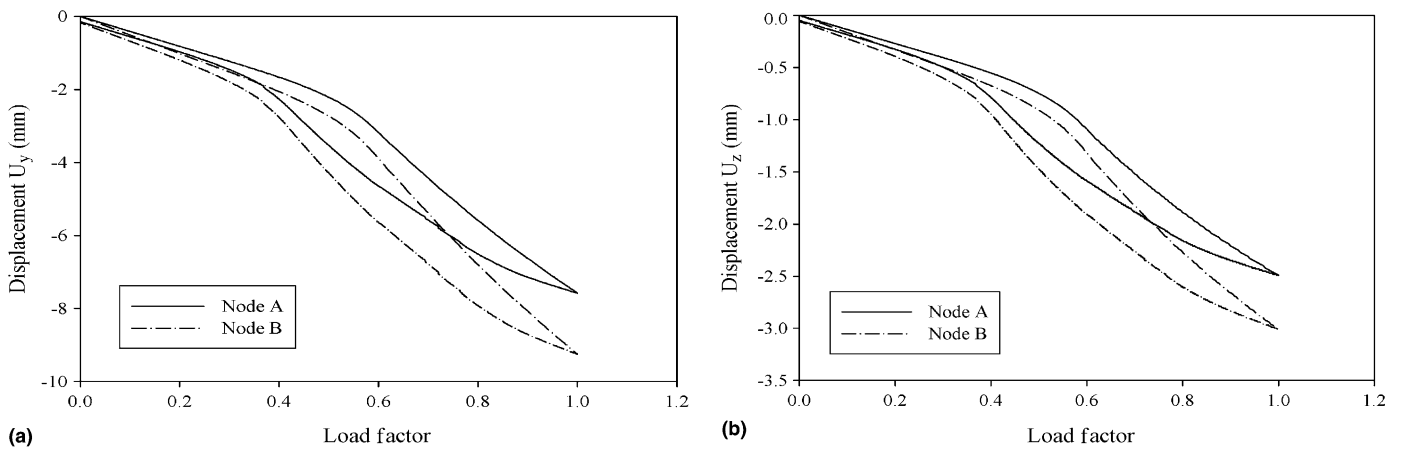


Fig. 18. Load–deflection U_y (a) and U_z (b) for tetrahedra.

6.8. Cyclic loading of a cantilever beam

This simulation presents the load deflection response of a thin cantilever beam when subjected to cyclic loading. The geometry of the beam is: length = 40 mm, width = 2 mm, and depth = 8 mm. The mechanical material properties employed in the simulations are given in Table 3. The hexahedral mesh is composed of 16 elements along the length, 4 elements through the depth and 1 through the thickness, while the tetrahedra mesh is made by dividing the brick elements. For the case of brick elements the edge load as a function of pseudo-time is given in Fig. 19a, while the load–deflection response for the three load cycles is presented in Fig. 19b. Likewise, the load–time history and the load–deflection response for the tetrahedra mesh are presented in Fig. 20a and b, respectively.

Table 3
Material properties used in the simulation

Young's modulus	E	5000 MPa
Poisson's ratio	ν	0.35
Austenite start stress	S_{AS}	150 MPa
Austenite finish stress	S_{AF}	100 MPa
Martensite start stress	S_{MS}	150 MPa
Martensite finish stress	S_{MF}	200 MPa
Width of the hysteresis loop	e_L^T	0.06

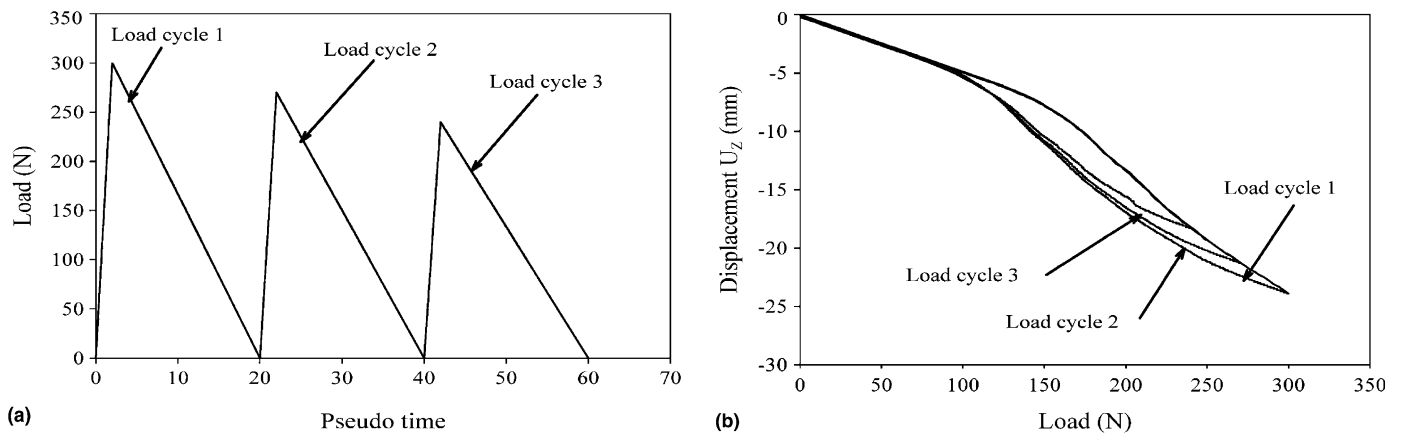


Fig. 19. (a) Load-time history for cyclic loading (Case I) and (b) load-deflection U_z for cyclic loading (8-node bricks).

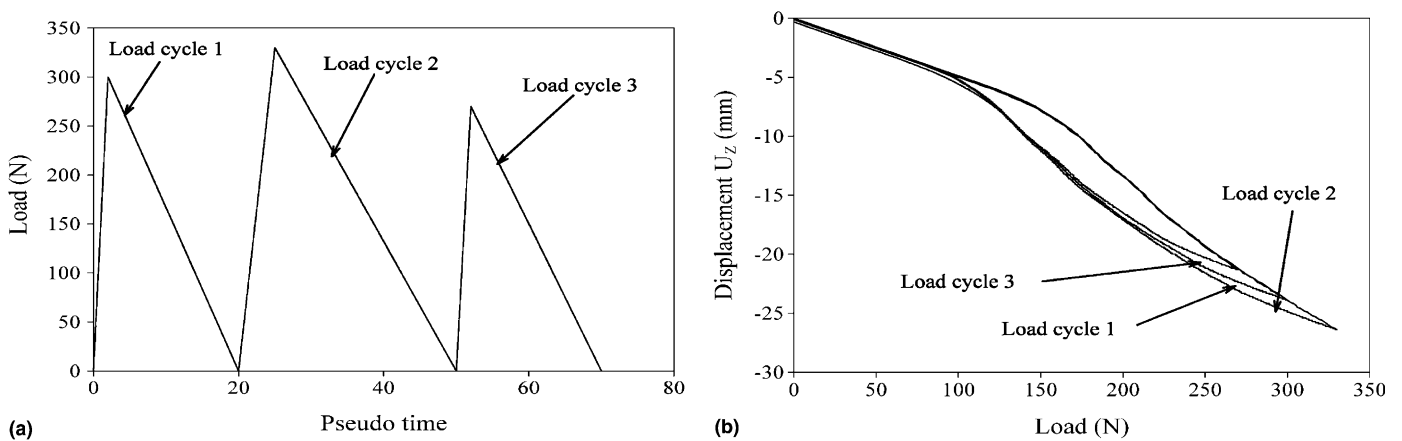


Fig. 20. (a) Load-time history for cyclic loading (Case II) and (b) load-deflection U_z for cyclic loading (4-node tetrahedra).

7. Conclusions

We have presented a new stabilized finite element method, termed as the HVM method, for small strain inelasticity. Specifically, a stabilized formulation that accommodates the nonlinear material behavior and the incompressibility constraint has been developed. This formulation allows arbitrary combinations of interpolation functions for the displacement and the pressure fields, and thus yields a family of stable and convergent elements. The novelty of the present method is that the structure of the stability tensors appears naturally in the derivations. Another important feature is that the fine computational scales are consistently represented in terms of the computable scales via the stabilization terms in the modified variational equation. Consequently, the proposed method naturally possesses better accuracy properties on cruder discretizations. This is a feature that is very attractive for large scale computations. Based on the formulation, a family of 2-D and 3-D elements is developed. These elements show a stable and convergent response while capturing the highly nonlinear behavior of shape memory alloys. An application of the proposed HVM method to materially nonlinear analysis and to elastoplasticity is straightforward.

Acknowledgements

The authors wish to thank Professor T.J.R. Hughes for helpful discussion. This work was supported by NSF grant NSF-CMS-9813386 and ONR grant N00014-02-1-0143. This support is gratefully acknowledged.

References

- [1] F. Auricchio, R.L. Taylor, J. Lubliner, Shape-memory alloys: macromodelling and numerical simulations of the superelastic behavior, *Comput. Methods Appl. Mech. Engrg.* 146 (1997) 281–312.

- [2] C. Baiocchi, F. Brezzi, L. Franca, Virtual bubbles and Galerkin/Least-squares type methods (Ga.L.S.), *Comput. Methods Appl. Mech. Engrg.* 105 (1993) 125–141.
- [3] T. Belytschko, L.P. Bindeman, Assumed strain stabilization of the 4-node quadrilateral with 1-point quadrature for nonlinear problems, *Comput. Methods Appl. Mech. Engrg.* 88 (1991) 311–340.
- [4] F. Brezzi, M.O. Bristeau, L.P. Franca, M. Mallet, G. Roge, A relationship between stabilized finite element methods and the Galerkin method with bubble functions, *Comput. Methods Appl. Mech. Engrg.* 96 (1992) 117–129.
- [5] A.N. Brooks, T.J.R. Hughes, Streamline upwind/Petrov–Galerkin methods for convection dominated flows with particular emphasis on the incompressible Navier–Stokes equations, *Comput. Methods Appl. Mech. Engrg.* 32 (1982) 199–259.
- [6] L.C. Brinson, One-dimensional constitutive behavior of shape memory alloys: thermomechanical derivation with non-constant material functions and redefined martensite internal variables, *J. Intell. Mater. Syst. Struct.* 4 (1993) 229–242.
- [7] L.C. Brinson, S. Hwang, Simplifications and comparisons of shape memory alloy constitutive models, *J. Intell. Mater. Syst. Struct.* 7 (1996) 108–114.
- [8] S. Commend, A. Truty, T. Zimmermann, Stabilized finite elements applied to elastoplasticity: I. Mixed displacement–pressure formulation, *Comput. Methods Appl. Mech. Engrg.* 193 (2004) 3559–3586.
- [9] K. Garikipati, T.J.R. Hughes, A variational multiscale approach to strain localization–formulation for multidimensional problems, *Comput. Methods Appl. Mech. Engrg.* 188 (2000) 39–60.
- [10] T.J.R. Hughes, *The Finite Element Method: Linear Static and Dynamic Finite Element Analysis*, Prentice-Hall, Englewoods Cliffs, NJ, 1987, Dover edition, 2000.
- [11] T.J.R. Hughes, Multiscale phenomena: Green’s functions, the Dirichlet-to-Neumann formulation, subgrid scale models, bubbles and the origins of stabilized methods, *Comput. Methods Appl. Mech. Engrg.* 127 (1995) 387–401.
- [12] T.J.R. Hughes, Generalization of selective integration procedures to anisotropic and nonlinear media, *Int. J. Numer. Methods Engrg.* 15 (1980) 1413–1418.
- [13] T.J.R. Hughes, A. Brooks, A theoretical framework for Petrov–Galerkin methods with discontinuous weighting functions: applications to the streamline upwind procedure, in: R.H. Gallagher, G.F. Carey, J.T. Oden, O.C. Zienkiewicz (Eds.), *Finite Elements in Fluids*, vol. IV, Wiley, Chichester, 1982, pp. 46–65.
- [14] T.J.R. Hughes, L.P. Franca, A new finite element formulation for computational fluid dynamics: VII. The Stokes problem with various well-posed boundary conditions: symmetric formulations that converge for all velocity/pressure spaces, *Comput. Methods Appl. Mech. Engrg.* 65 (1987) 85–96.
- [15] T.J.R. Hughes, L.P. Franca, M. Balestra, A new finite element formulation for computational fluid dynamics: V. Circumventing the Babuska–Brezzi condition: a stable Petrov–Galerkin formulation of the stokes problem accommodating equal-order interpolations, *Comput. Methods Appl. Mech. Engrg.* 59 (1986) 85–99.
- [16] T.J.R. Hughes, L.P. Franca, G.M. Hulbert, A new finite element formulation for computational fluid dynamics: VIII. The Galerkin/least-squares method for advective–diffusive equations, *Comput. Methods Appl. Mech. Engrg.* 73 (1989) 173–189.
- [17] T.J.R. Hughes, D.S. Malkus, A general penalty/mixed equivalence theorem for anisotropic, incompressible finite elements, in: S.N. Atluri, R.H. Gallaher, O.C. Zienkiewicz (Eds.), *Hybrid and Mixed Finite Element Methods*, John Wiley, London, 1983, pp. 487–496.
- [18] O. Klaas, A.M. Maniatty, M.S. Shephard, A stabilized mixed Petrov–Galerkin finite element method for finite elasticity. formulation for linear displacement and pressure interpolation, *Comput. Methods Appl. Mech. Engrg.* 180 (1999) 65–79.
- [19] C. Lexcellent, S. Leclercq, B. Gabry, G. Bourbon, The two way shape memory effect of shape memory alloys: an experimental study and a phenomenological model, *Int. J. Plast.* 16 (2000) 1155–1168.
- [20] J. Lubliner, F. Auricchio, Generalized plasticity and shape memory alloys, *Int. J. Solids Struct.* 33 (1996) 991–1003.
- [21] D.S. Malkus, T.J.R. Hughes, Mixed finite element methods-reduced and selective integration techniques: a unification of concepts, *Comput. Methods Appl. Mech. Engrg.* 15 (1) (1987) 63–81.
- [22] A. Masud, Stabilized methods in solid mechanics, in: L.P. Franca, T.E. Tezduyar, A. Masud (Eds.), *Finite Element Methods: 1970’s and Beyond*, CIMNE, Barcelona, Spain, 2004, pp. 172–187.
- [23] A. Masud, M. Panahandeh, F. Auricchio, A finite deformation finite element model for the pseudoelastic behavior of shape memory alloys, *Comput. Methods Appl. Mech. Engrg.* 148 (1997) 23–37.
- [24] A. Masud, K. Xia, A stabilized mixed finite element method for nearly incompressible elasticity, *J. Appl. Mech.* 72 (2005) 711–720.
- [25] I. Muller, H. Xu, On the pseudo-elastic hysteresis, *Acta Metall. Mater.* 39 (1991) 263–271.
- [26] M. Ortiz, J.C. Simo, An analysis of a new class of integration algorithms for elastoplastic constitutive relations, *Int. J. Numer. Methods Engrg.* 23 (1986) 353–366.
- [27] M.A. Qidwai, D.C. Lagoudas, Numerical implementation of a shape memory alloy thermomechanical constitutive model using return mapping algorithms, *Int. J. Numer. Methods Engrg.* 47 (2000) 1123–1168.
- [28] K.R. Rajagopal, A.R. Srinivasa, On the inelastic behavior of solids. Part I. Twinning, *Int. J. Plast.* 11 (1995) 653–678.
- [29] J.C. Simo, T.J.R. Hughes, *Computational Inelasticity*, Springer-Verlag, 1997.
- [30] J.C. Simo, M.S. Rifai, A class of mixed assumed strain methods and the method of incompatible modes, *Int. J. Numer. Methods Engrg.* 29 (1990) 1595–1636.
- [31] J.C. Simo, R.L. Taylor, K.S. Pister, Variational and projection methods for the volume constraint in finite deformation elasto-plasticity, *Comput. Methods Appl. Mech. Engrg.* 51 (1985) 177–208.